

## Supporting Information

for *Adv. Sci.*, DOI 10.1002/adv.202413518

Nitric Oxide-Releasing Nanoscale Metal-Organic Layer Overcomes Hypoxia and Reactive Oxygen Species Diffusion Barriers to Enhance Cancer Radiotherapy

*Yuxuan Xiong, Jinhong Li, Xiaomin Jiang, Wenyao Zhen, Xin Ma and Wenbin Lin\**

## Supporting Information

### **Nitric Oxide-Releasing Nanoscale Metal-Organic Layer Overcomes Hypoxia and Reactive Oxygen Species Diffusion Barriers to Enhance Cancer Radiotherapy**

*Yuxuan Xiong, Jinhong Li, Xiaomin Jiang, Wenyao Zhen, Xin Ma, Wenbin Lin\**

Y. Xiong, J. Li, X. Jiang, W. Zhen, X. Ma, W. Lin

Department of Chemistry

The University of Chicago

Chicago, IL 60637, USA

E-Mail: wenbinlin@uchicago.edu

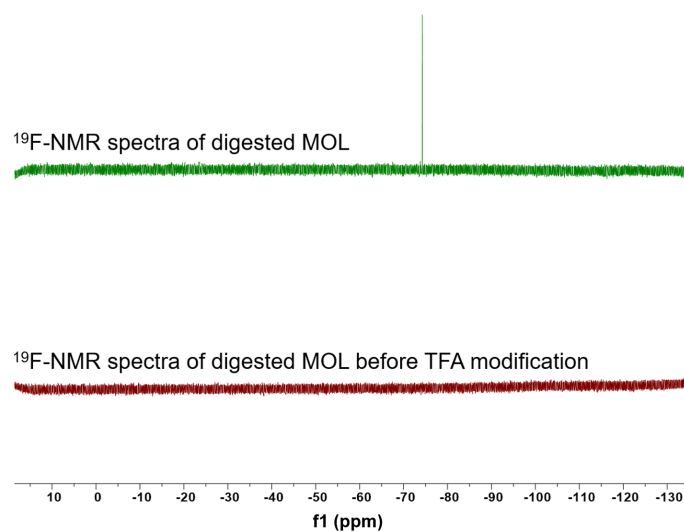
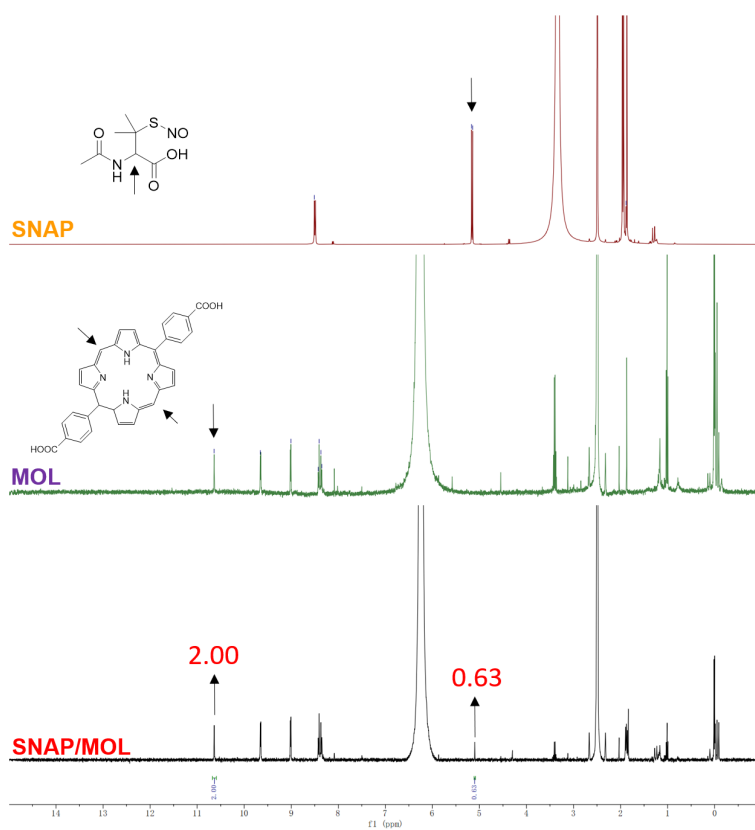
W. Lin

Department of Radiation and Cellular Oncology and the Ludwig Center for Metastasis Research

The University of Chicago

Chicago, IL 60637, USA

## Supplementary Figures

**Figure S1.** <sup>19</sup>F-NMR spectra of the digested MOL before and after TFA modification.**Figure S2.** <sup>1</sup>H-NMR spectra of SNAP, digested MOL, and digested SNAP/MOL.

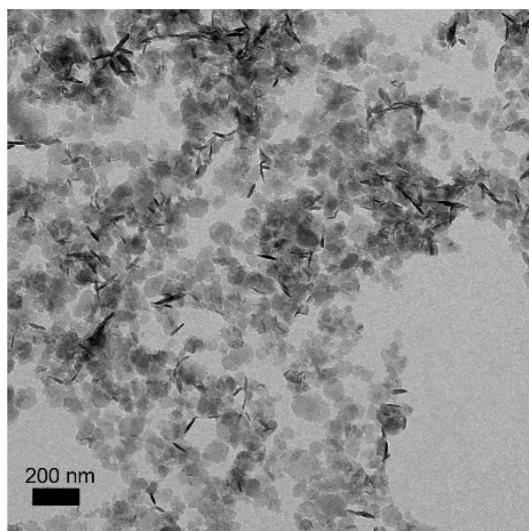


**Figure S3.** TEM image of three dimensional MOF.

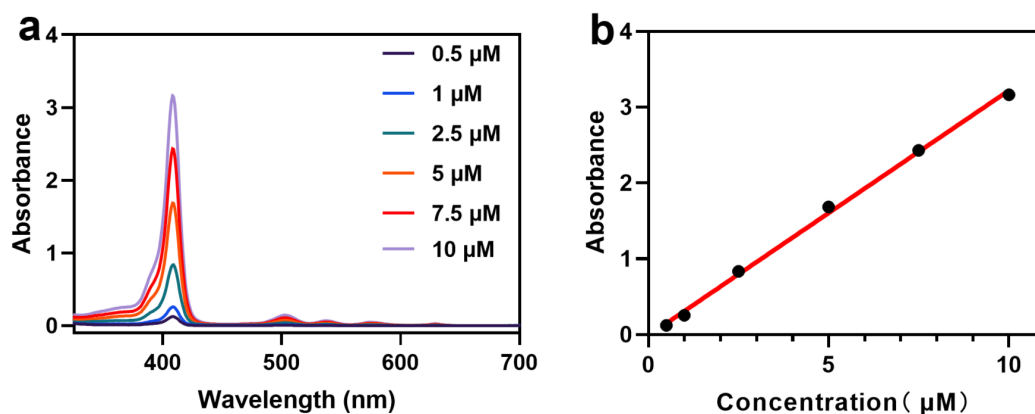


**Figure S4.** (a) UV-Vis absorption spectra of H<sub>2</sub>DBP at various concentrations in DMSO with 10% H<sub>3</sub>PO<sub>4</sub>. (b) The linear fit of H<sub>2</sub>DBP absorbance at 408 nm as a function of concentration.

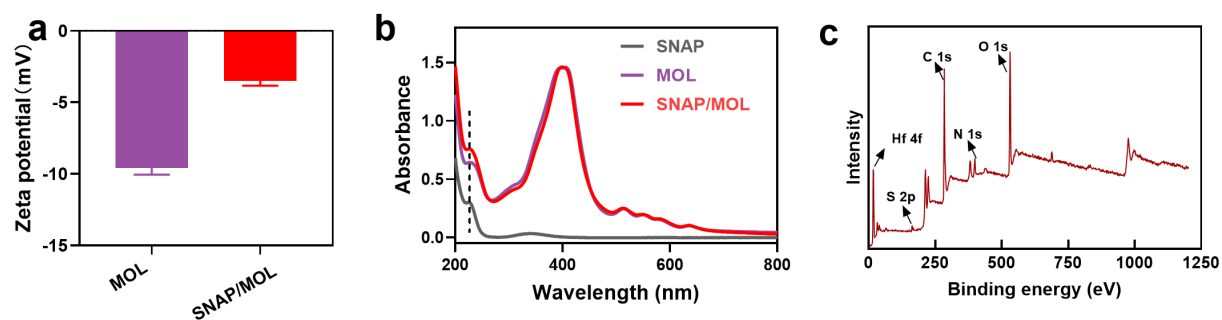


**Figure S5.** (a) Zeta potential values of MOL and SNAP/MOL ( $n=5$ , data are shown as mean  $\pm$  SD). (b) UV-Vis spectrum of SNAP, MOL and SNAP/MOL. (c) XPS spectrum of SNAP/MOL.

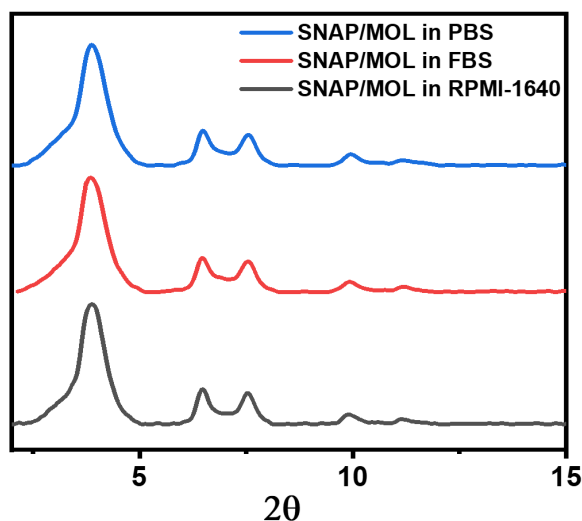


**Figure S6.** PXRD patterns of SNAP/MOL after incubation in biologically relevant media.

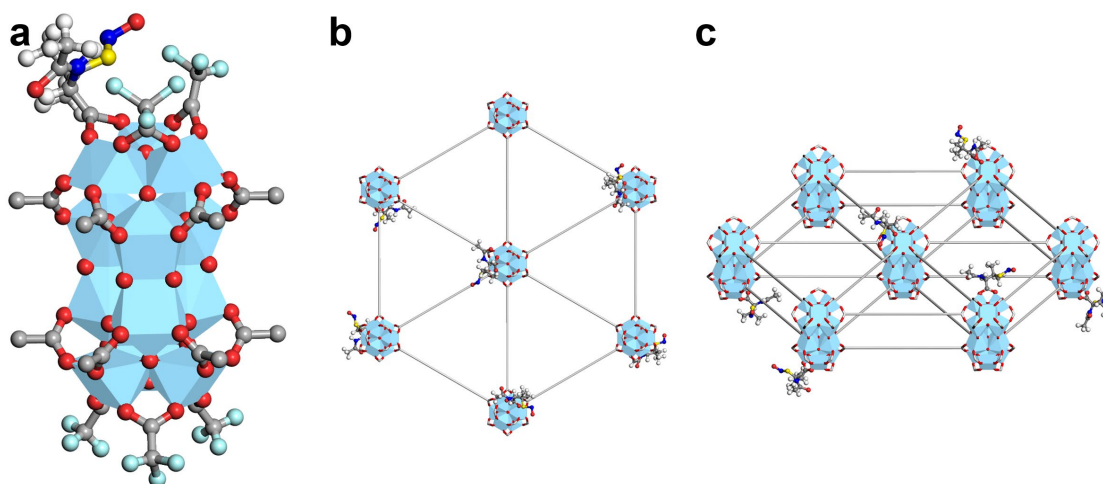


**Figure S7.** Structure models of SNAP/MOL. (a) The structure of mono-substituted  $\text{Hf}_{12}(\mu_3\text{-O})_8(\mu_3\text{-OH})_8(\mu_2\text{-OH})_6(\text{DBP})_6(\mu_2\text{-TFA})_{2.4}(\mu_2\text{-SNAP})_{3.6}$ . (b) The top view of SNAP/MOL reveals its monolayer structure. (c) Side view of SNAP/MOL. Light blue: Hf; red: O; navy blue: N.

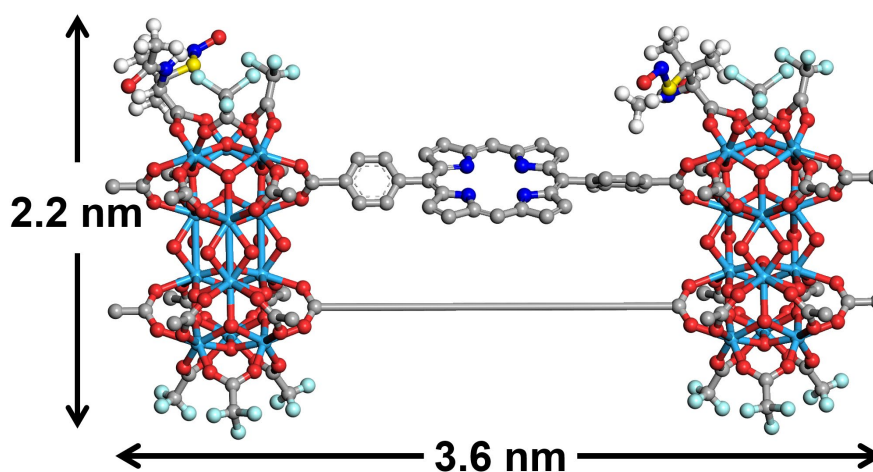


**Figure S8.** Size information and topological structure of SNAP- $\text{Hf}_{12}$ -DBP unit.

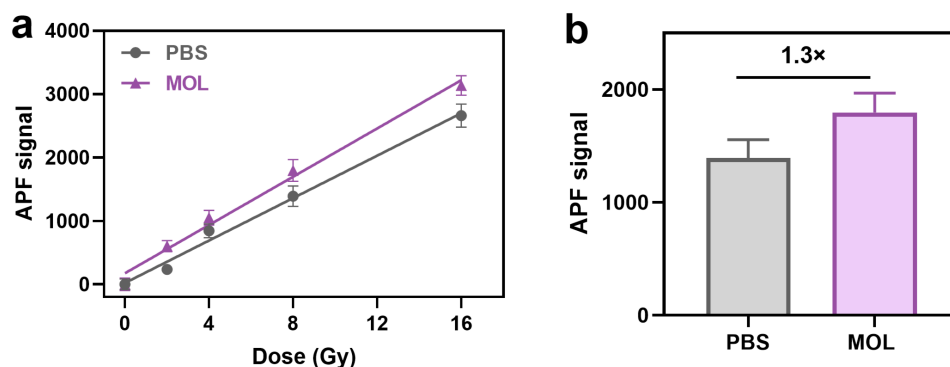


**Figure S9.** (a) Hydroxyl radical signal of PBS and MOL by APF assay after different doses of X-ray. (b) Fluorescence intensity of APF at 528 nm after 8 Gy X-ray irradiation (n=3). All data are shown as mean $\pm$ SD.

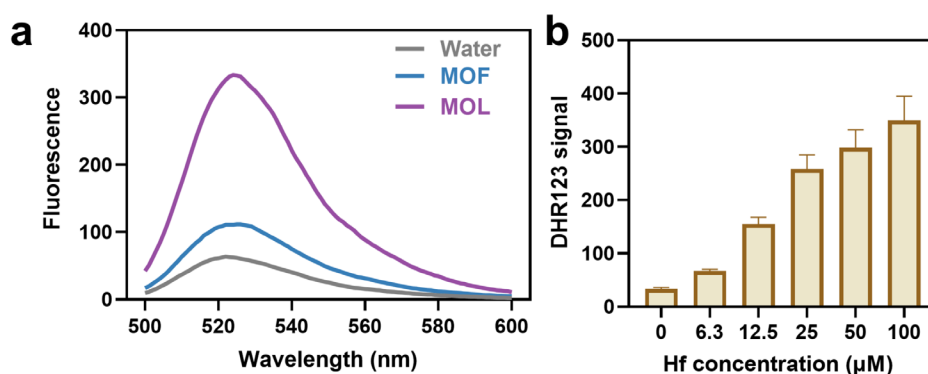


**Figure S10.** (a) Superoxide generation by MOL and MOF (40  $\mu$ M Hf) under the irradiation of 8 Gy X-ray, using DHR123 as probe. (b) DHR123 signals of different concentrations of MOL under X-ray radiation (n=3, data are shown as mean $\pm$ SD).

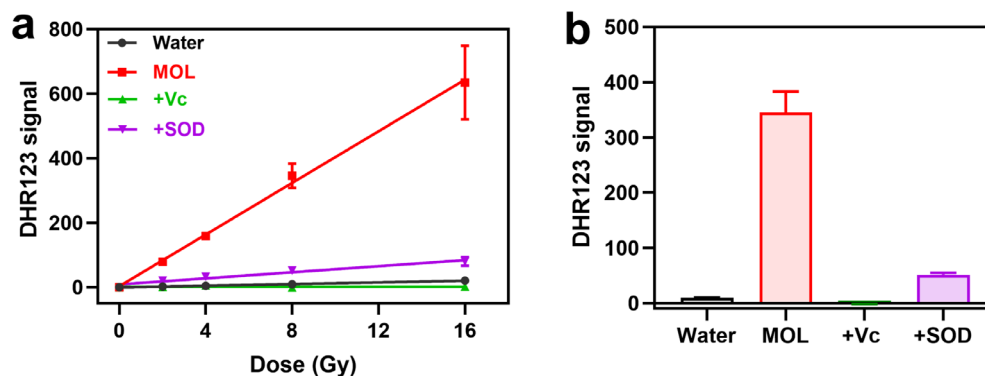


**Figure S11.** (a) DHR123 signals of MOL co-incubated with SOD (50  $\mu$ g/mL) or Vc (50  $\mu$ M) at different doses of X-ray irradiation. (b) DHR123 fluorescence intensities at 528 nm after 8 Gy X-ray irradiation. All data are shown as mean $\pm$ SD, n=5.

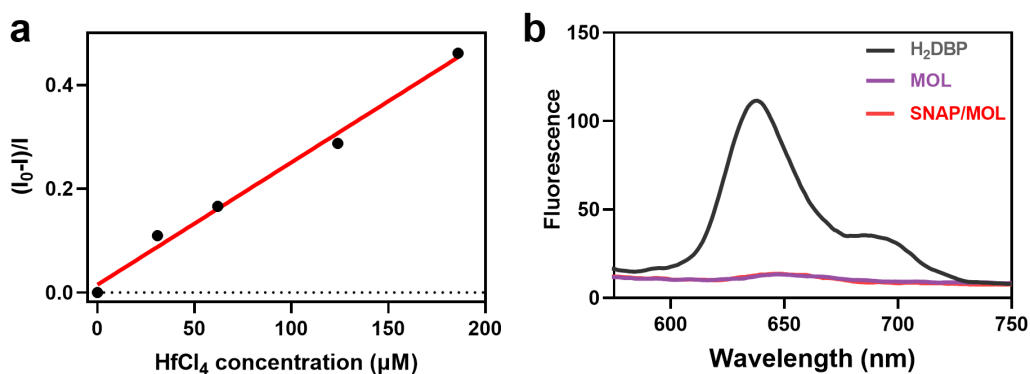


**Figure S12.** (a) Plots of  $(I_0 - I)/I$  as a function of the concentration of  $\text{HfCl}_4$ . (b) Fluorescence of  $\text{H}_2\text{DBP}$ , MOL and SNAP/MOL with a DBP concentration of  $20 \mu\text{M}$  ( $\text{Ex}=405 \text{ nm}$ ).

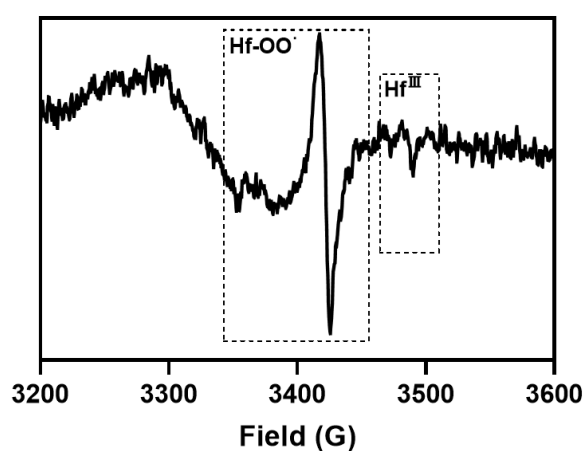


**Figure S13.** EPR spectrum of  $\text{Hf}(\text{O}_2)\text{-DBP}$ , showing strong superoxide and  $\text{Hf}^{\text{III}}$  signal.

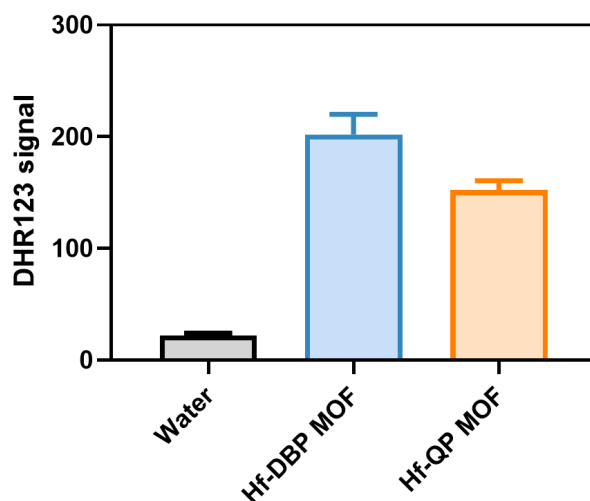


**Figure S14.** Superoxide generation by Hf-DBP MOF and Hf-QP MOF ( $40 \mu\text{M}$  Hf) under X-ray irradiation. QP is amide-quaterphenyldicarboxylic acid, a ligand without photosensitizing properties. All data are shown as mean  $\pm$  SD,  $n=3$ .

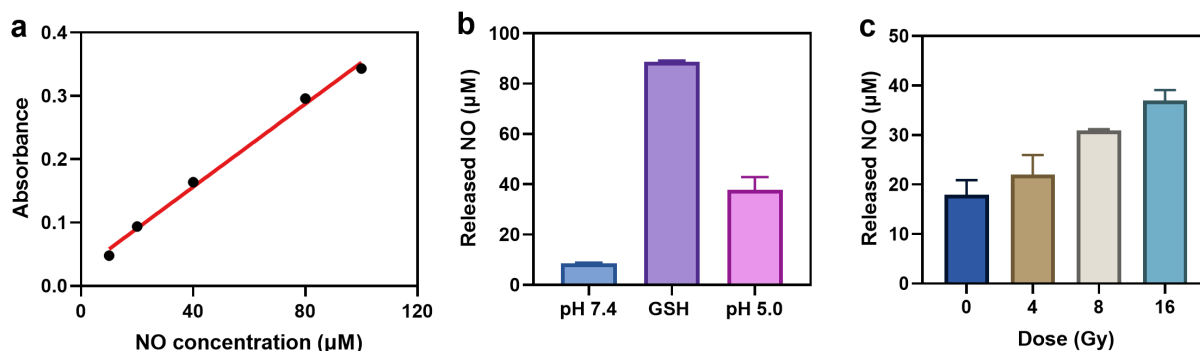


**Figure S15.** (a) NO standard curve obtained by Griess reagent test. (b) NO release from SNAP in different microenvironments.  $n=3$ . (c) NO release from SNAP/MOL after exposure to different doses of X-ray.  $n=3$ , all data are shown as mean  $\pm$  SD.

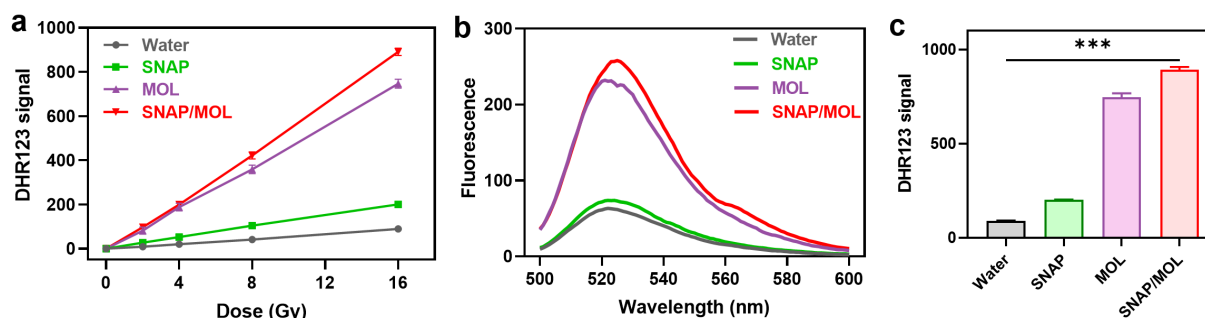


**Figure S16.** (a) DHR123 signals of SNAP, MOL, and SNAP/MOL at different doses of X-ray irradiation. ( $n=3$ ) (b) Fluorescence spectra of DHR123 with different treatments. The Hf concentration was 40  $\mu$ M, with 8 Gy X-ray irradiation. (c) DHR123 fluorescence intensities at 528 nm after 16 Gy X-ray irradiation.  $n=3$ , data are shown as mean  $\pm$  SD. SNAP-induced enhancement of DHR123 signal may be due to the generation of ONOO $^-$ .

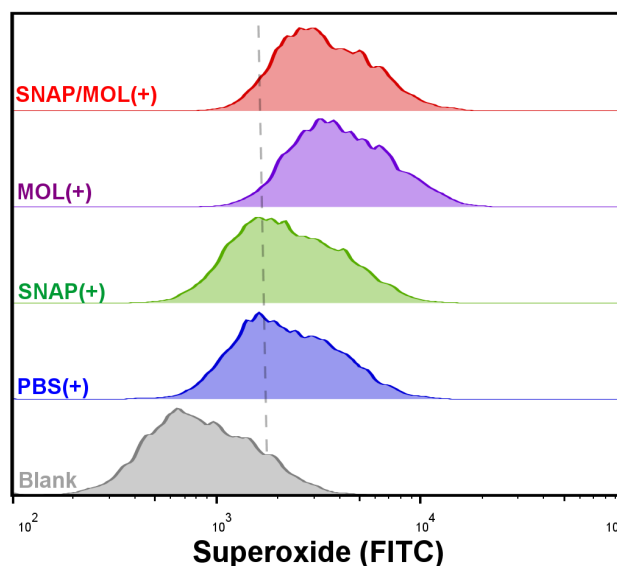


**Figure S17.** Fluorescence histograms showing superoxide generation in 4T1 cells under X-ray irradiation.

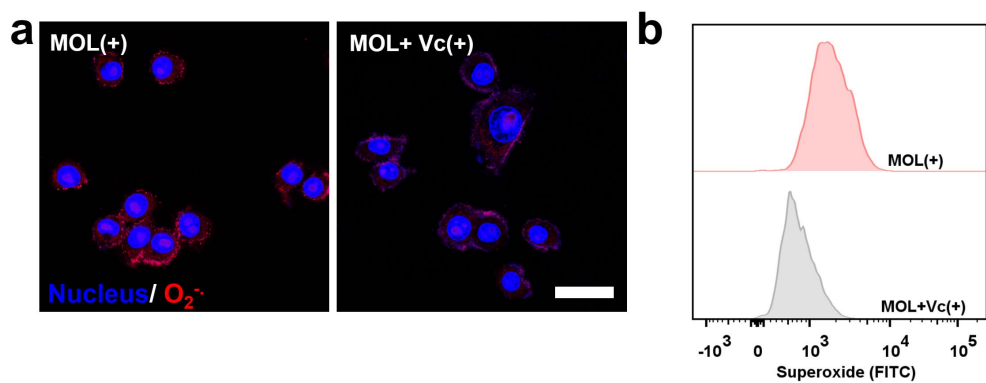


**Figure S18.** Confocal images (a) and flow cytometric analysis (b) showing the quenching of superoxide signals by Vc. Scale bar, 20  $\mu$ m.

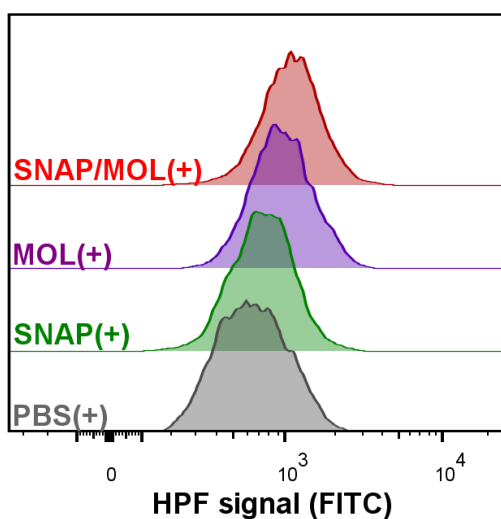


**Figure S19.** Fluorescence histograms showing hydroxyl radical generation under X-ray irradiation probed by HPF probe.

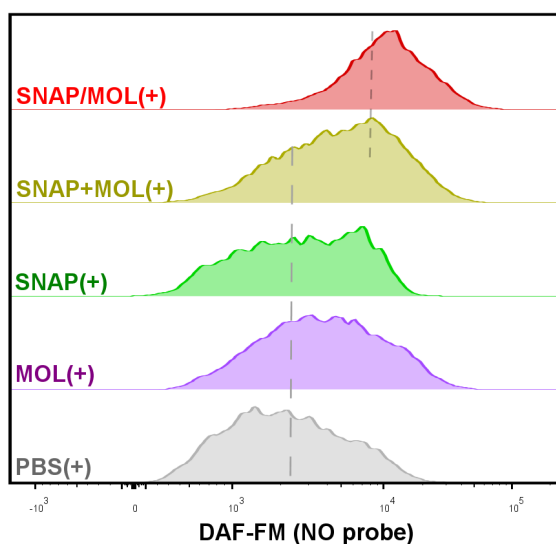


**Figure S20.** Fluorescence histograms showing NO generation in 4T1 cells under X-ray irradiation as probed by DAF-FA DA.

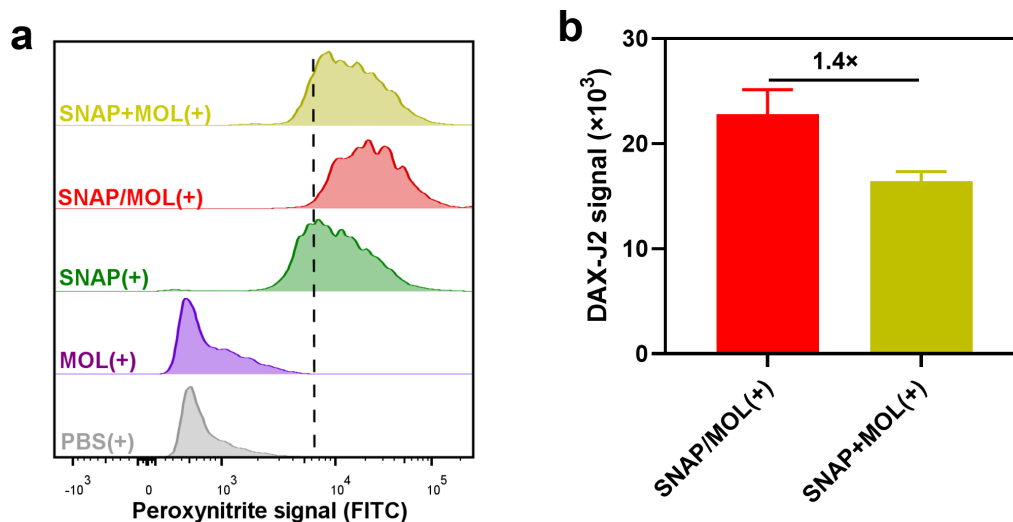


**Figure S21.** (a) Fluorescence histograms of intracellular peroxynitrite signals by flow cytometry using DAX-J2 probe. (b) Intracellular DAX-J2 signal intensity statistics after SNAP/MOL(+) and SNAP + MOL(+) treatments (n=3, data are shown as mean $\pm$ SD).

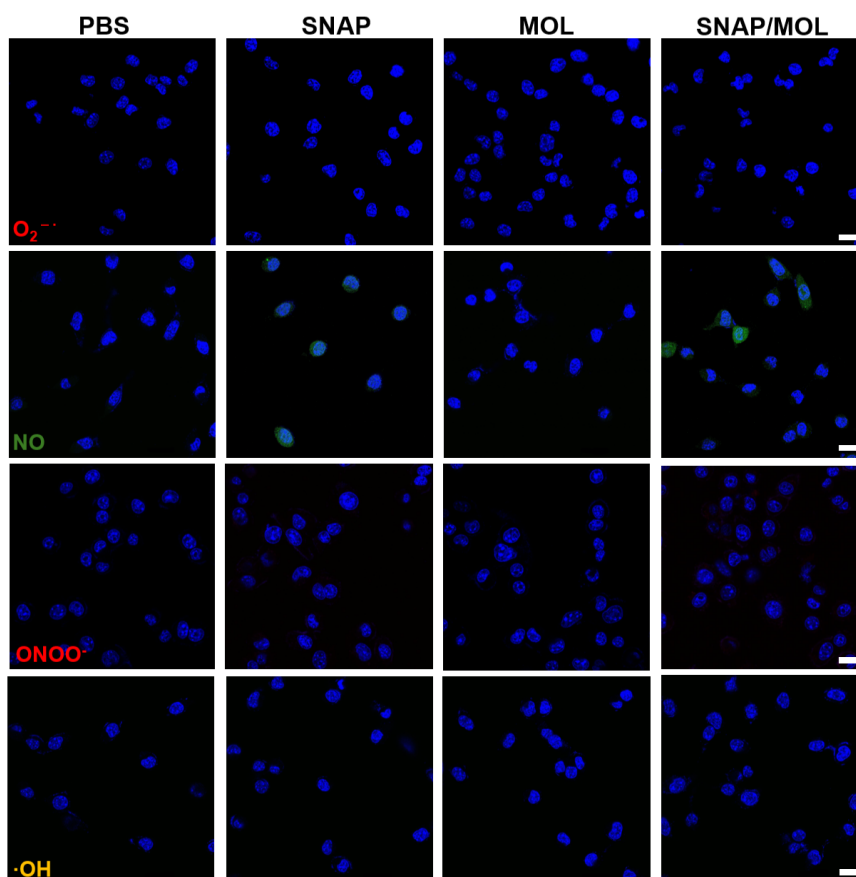


**Figure S22.** CLSM images of (a)  $O_2^{\cdot-}$ , (b) NO, (c)  $ONOO^{\cdot-}$  and (d)  $\cdot OH$  staining of different groups without X-ray irradiation. The nuclei were visualized with Hoechst 33342 (blue). The scale bars are 20  $\mu m$ .

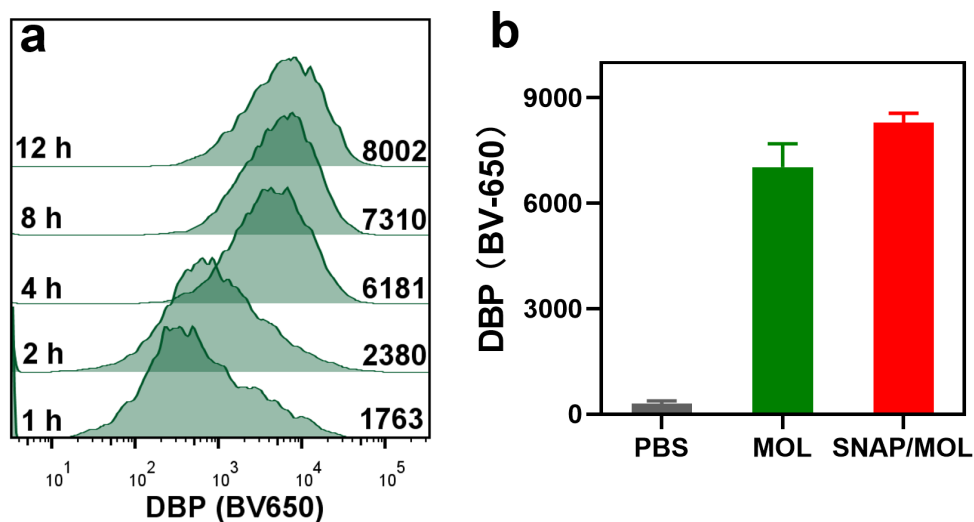


**Figure S23.** (a) Time-dependent uptake of SNAP/MOL in 4T1 cells via flow cytometric analysis of DBP fluorescence. (b) DBP fluorescence intensities after 12-hour incubation of 4T1 cells with MOL and SNAP/MOL by flow cytometry ( $n=3$ , data are shown as mean $\pm$ SD).

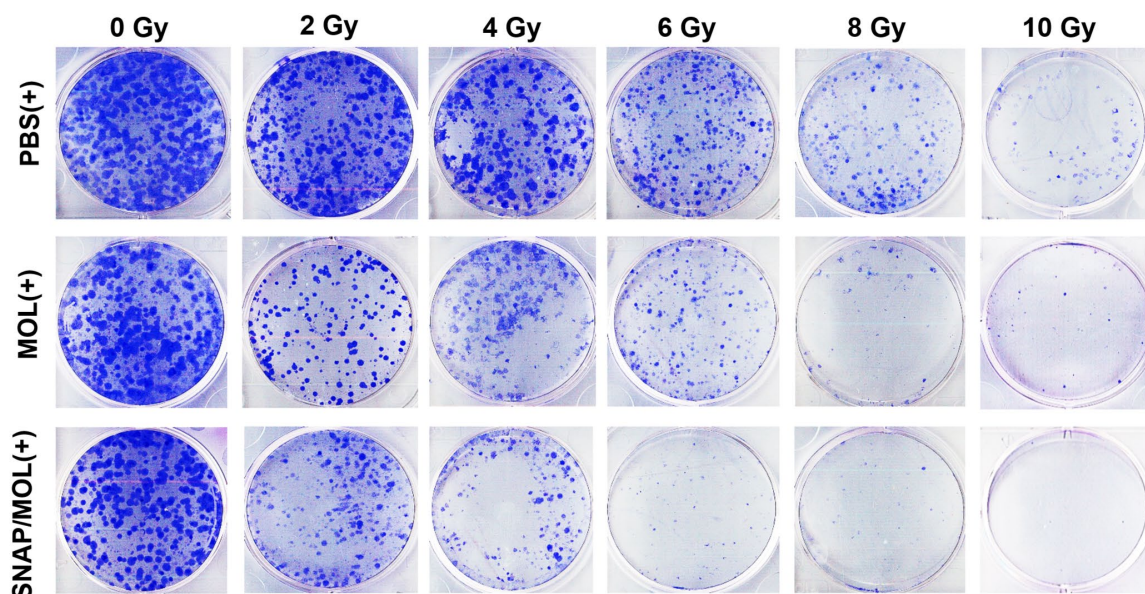


**Figure S24.** Representative images of colonies formed by 4T1 cells treated with PBS, MOL, or SNAP/MOL under different doses of X-ray irradiation.

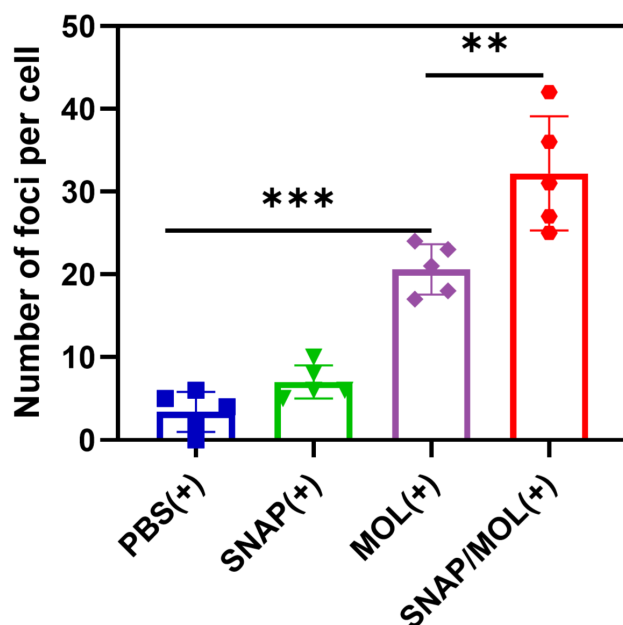


**Figure S25.** Statistical analysis of  $\gamma$ -H2AX assays showing DSBs in 4T1 cells after different treatments. All data are shown as mean  $\pm$  SD,  $n=3$ . Statistical significance was calculated via unpaired two-tailed student's  $t$  test. \*\*  $p < 0.01$ , \*\*\*  $p < 0.001$ .

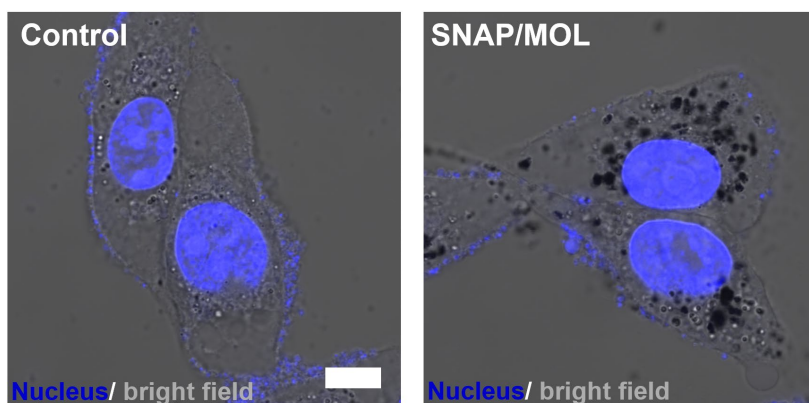


**Figure S26.** CLSM images showing the distribution of SNAP/MOL in 4T1 cells.

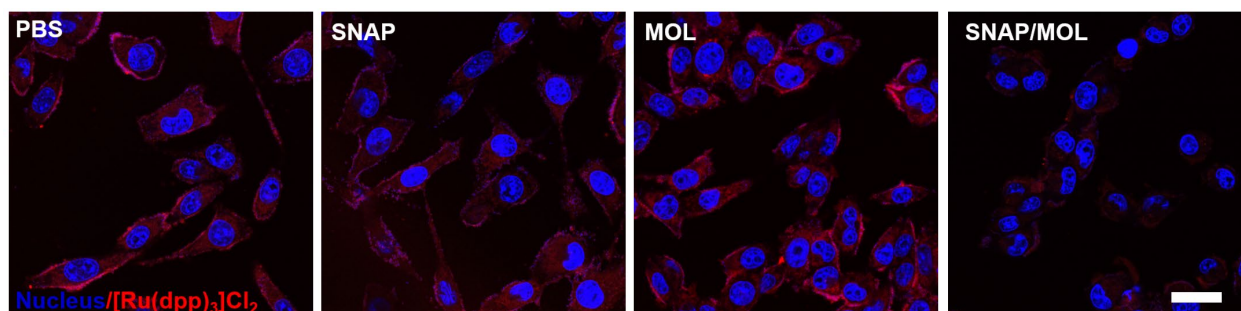


**Figure S27.** Confocal images of  $\text{Ru}(\text{dpp})_3\text{Cl}_2$  luminescence signals in 4T1 cells treated with SNAP, MOL and SNAP/MOL in a hypoxia chamber ( $p\text{O}_2 = 0.5$ ).

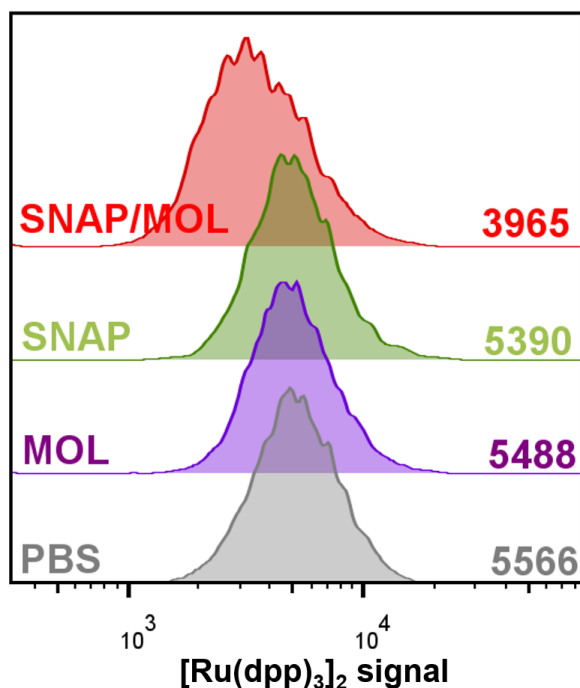


**Figure S28.** Histograms showing  $\text{Ru}(\text{dpp})_3\text{Cl}_2$  luminescence intensity in 4T1 cells with different treatments.

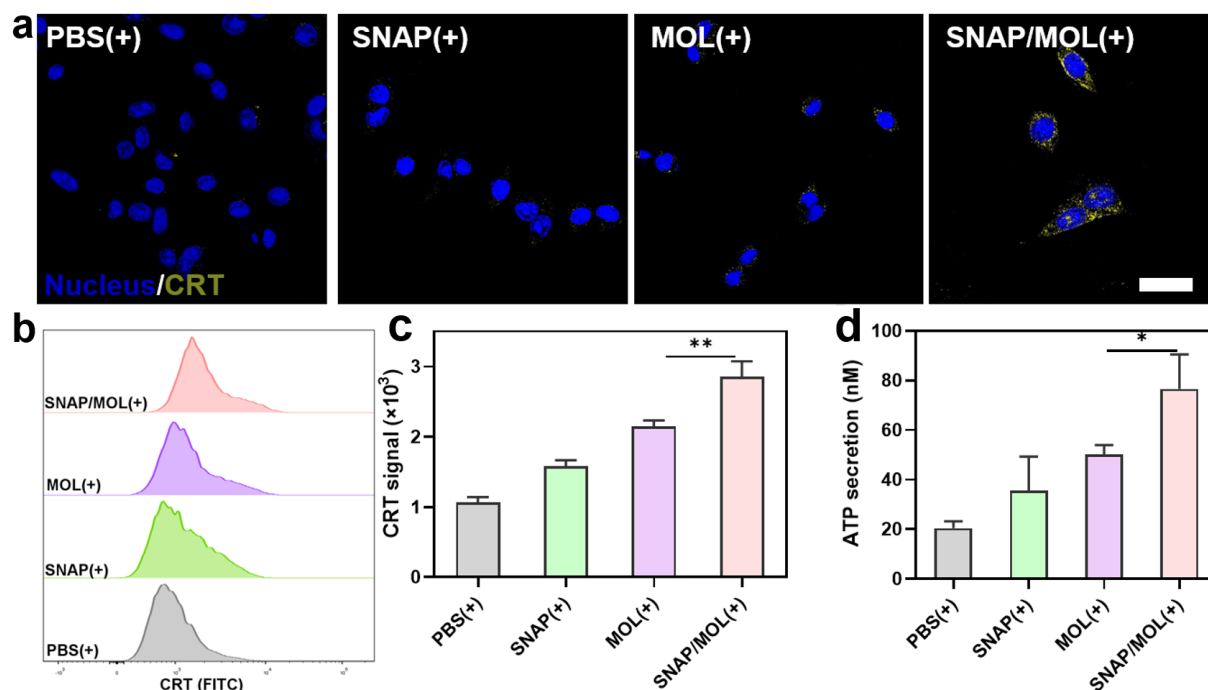


**Figure S29.** (a) CLSM images of surface translocation of CRT of 4T1 cells after different treatments. (b) Flow cytometric analysis of CRT expression on 4T1 cells 24 h after different treatments and (c) quantitative analysis of the corresponding CRT fluorescence intensities. (d) ATP secretion from 4T1 cells after indicated treatments measured by ATP Determination Kit.  $n=3$  for each experiment. All data are shown as mean  $\pm$  SD. Statistical significance was calculated via unpaired two-tailed student's t test. \*  $p<0.05$ , \*\*  $p<0.01$ .

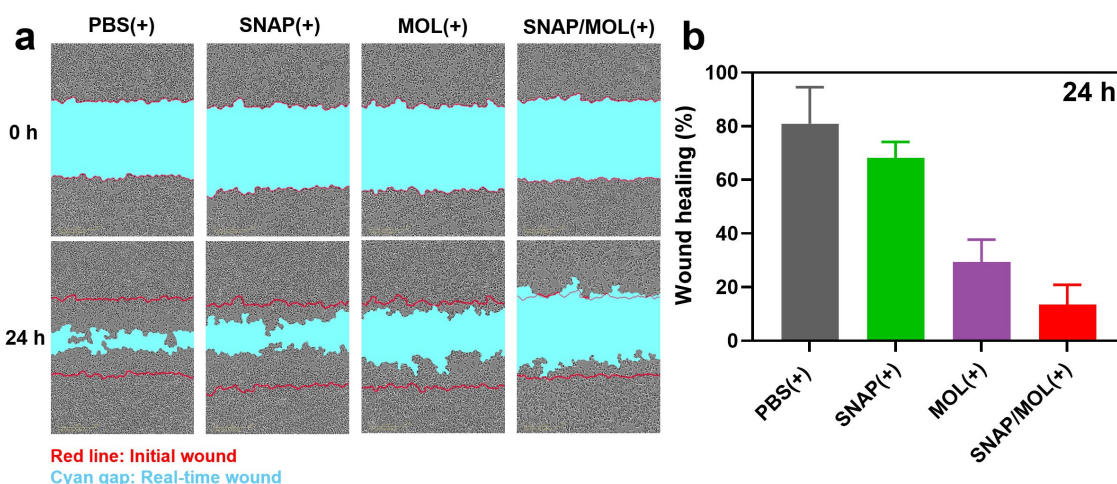


**Figure S30.** (a) Representative images of wound healing at 0 h and 24 h after radiation treatments. The initial wound is outlined in red, while the current wound is indicated by the cyan gap. (b) Statistical results of wound healing rate at 24 h (n=4). All data are shown as mean  $\pm$ SD.

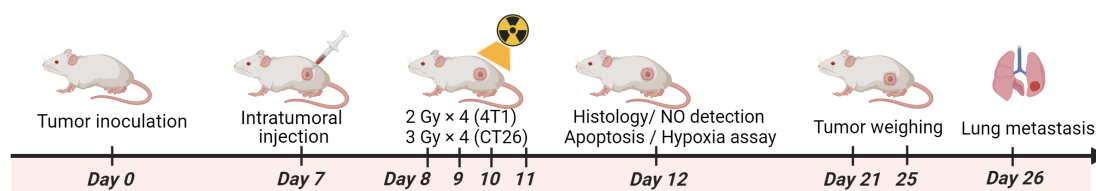


**Figure S31.** Experimental protocols for anti-tumor studies.

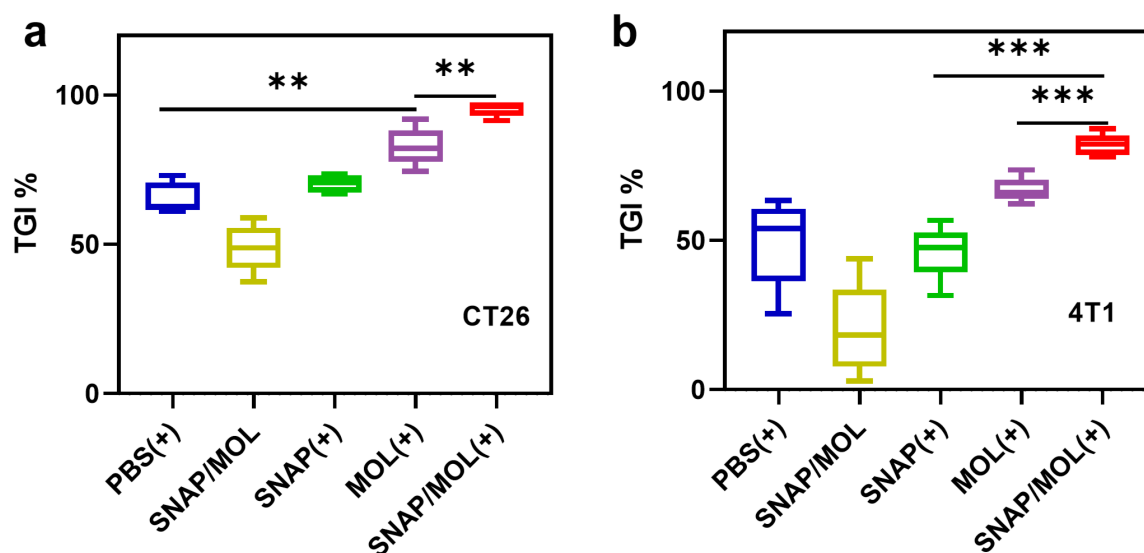


**Figure S32.** (a) Tumor growth inhibition (TGI) values of CT26 model calculated from tumor volume data on day 19. (b) TGI values of 4T1 model calculated from tumor volume data at the endpoint. n=5. All data are shown as mean  $\pm$ SD. Statistical significance was calculated via unpaired two-tailed student's t test. \*\* p < 0.01, \*\*\* p < 0.001.

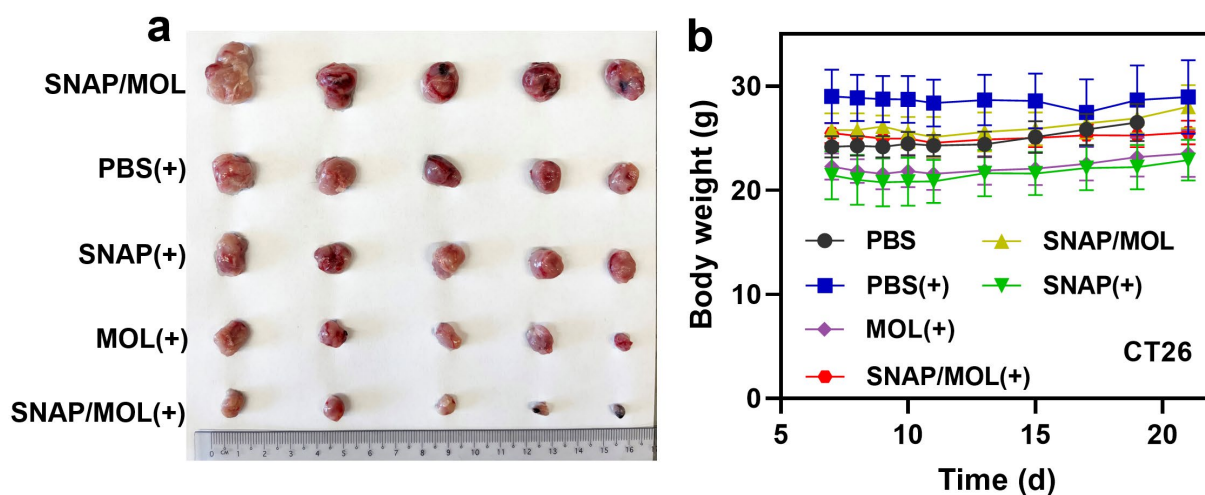


**Figure S33.** (a) *Ex vivo* images of CT26 tumors extracted from mice at the end of treatments. (b) Body weights of CT26 tumor-bearing mice during the treatment period.  $n=5$ . All data are shown as  $\text{mean} \pm \text{SD}$ .

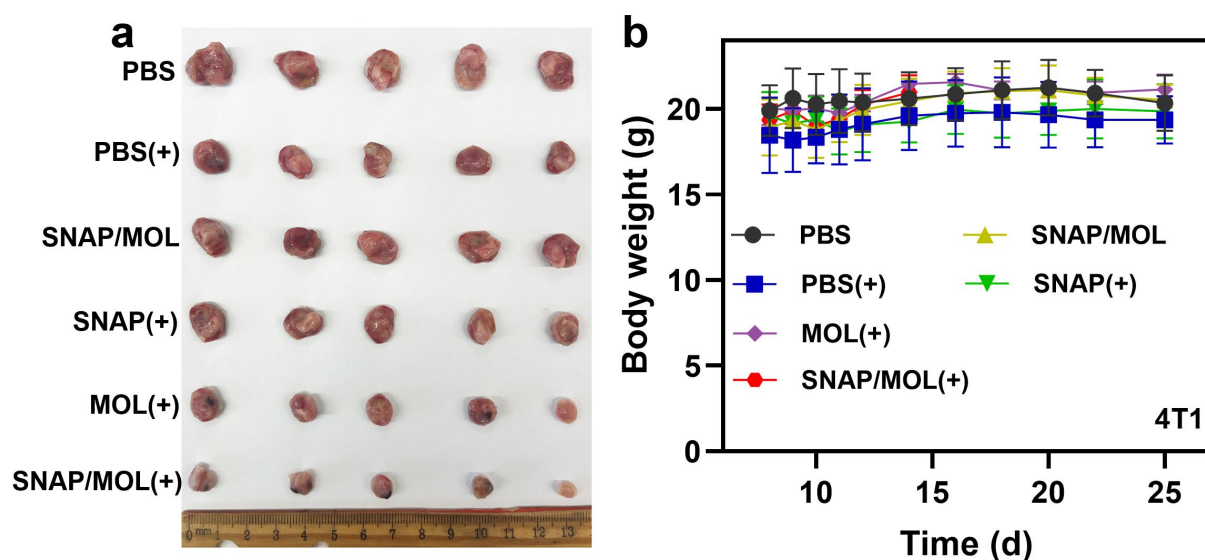


**Figure S34.** (a) *Ex vivo* images of 4T1 tumors extracted from mice at the end of treatments. (b) Body weights of 4T1 tumor-bearing mice during the treatment period.  $n=5$ . All data are shown as  $\text{mean} \pm \text{SD}$ .

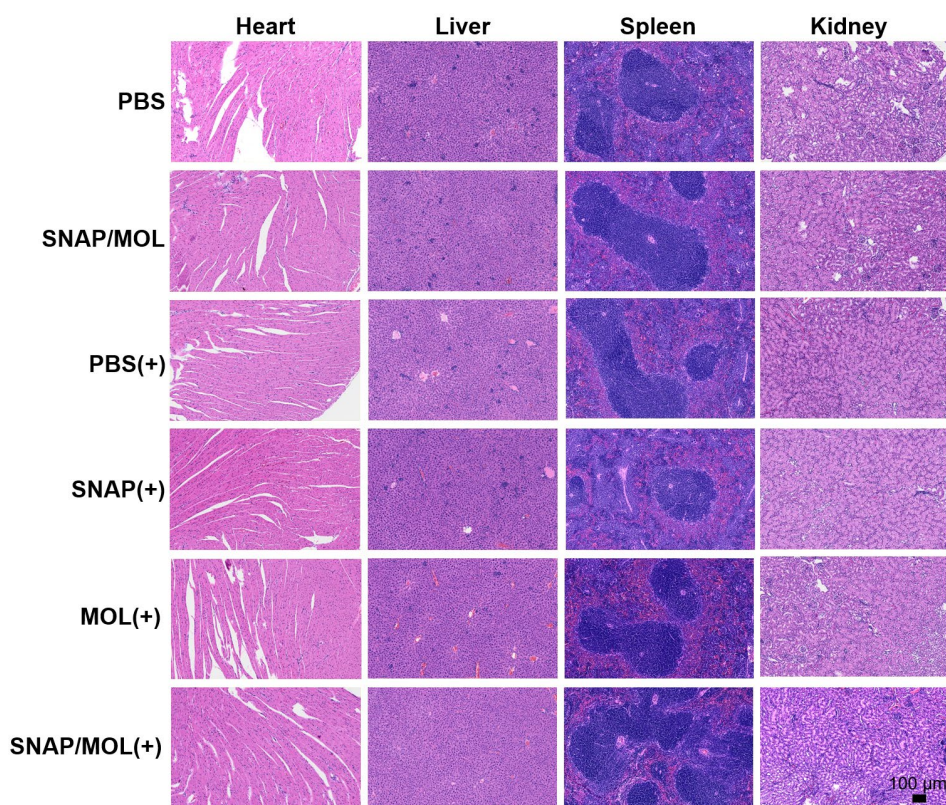


**Figure S35.** H&E sections of major organs of 4T1-bearing BALB/c mice.

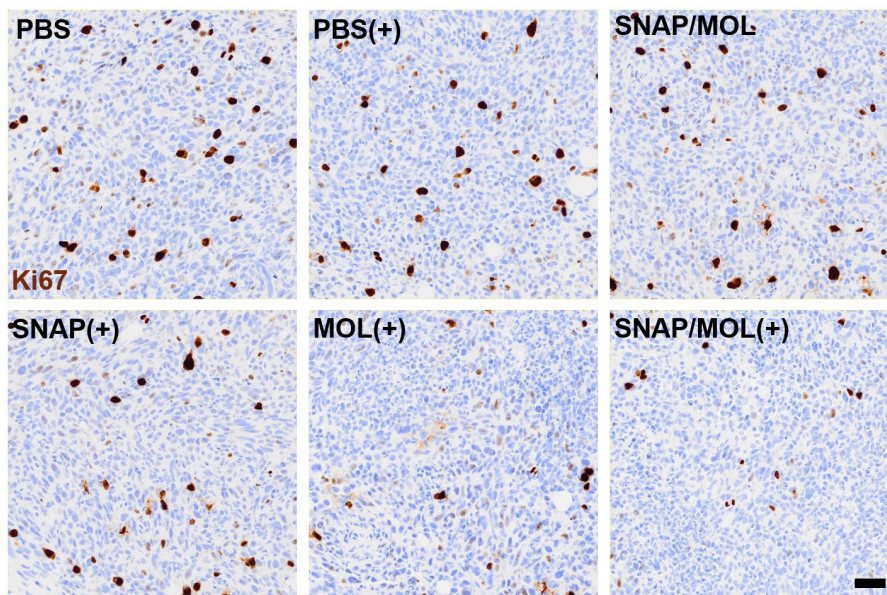


**Figure S36.** Immunohistochemistry of Ki67 staining of excised 4T1 tumors. Scale bars, 50 µm.

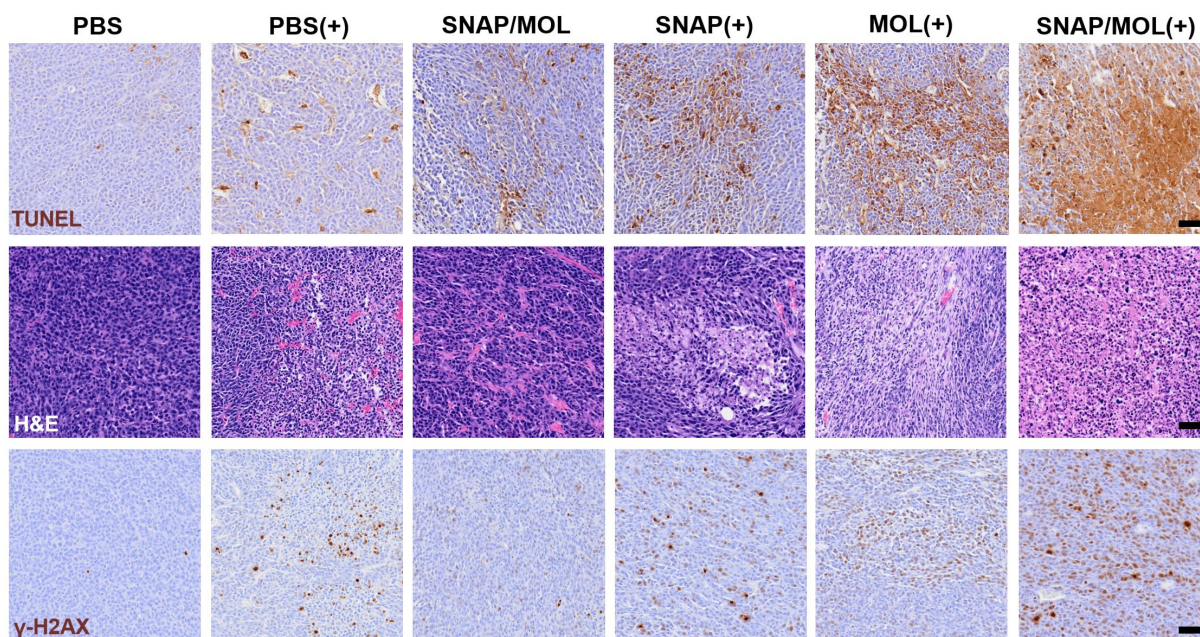


**Figure S37.** TUNEL, H&E and  $\gamma$ -H2AX staining of CT26 tumors resected after different treatments. Scale bars, 50  $\mu$ m. The results showed that SNAP/MOL(+) treatment induced intense apoptosis, severe necrosis, higher DNA damage on CT26 tumor modal.

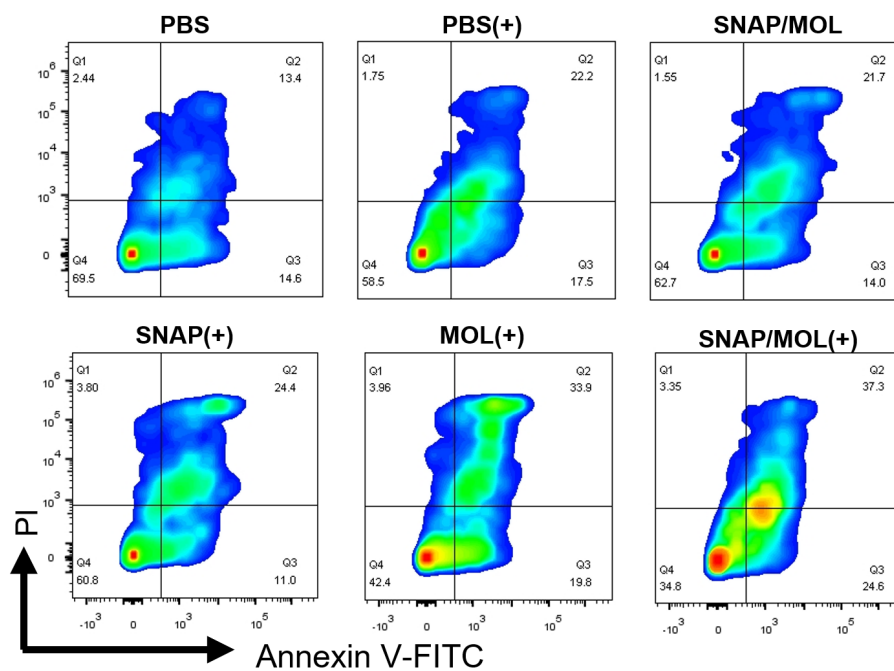


**Figure S38.** Assessment of apoptosis in 4T1 tumor tissues after different treatments.

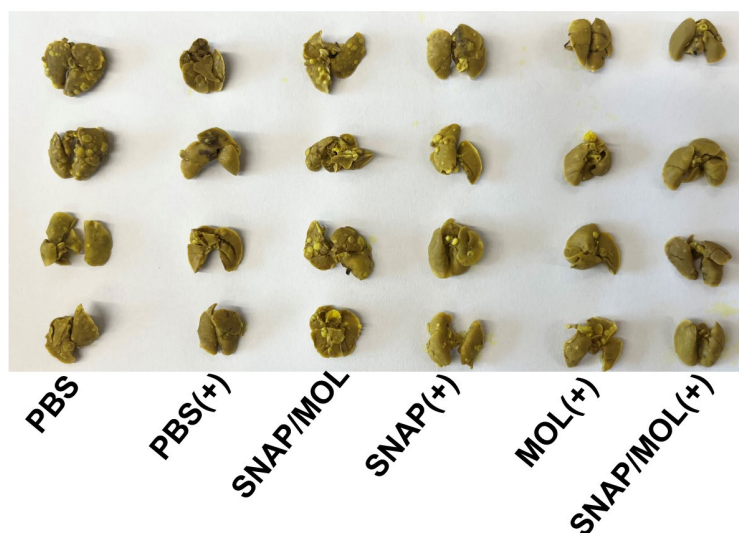


**Figure S39.** Photographs of the gross appearance of the tumor nodules in the lung after different treatments.

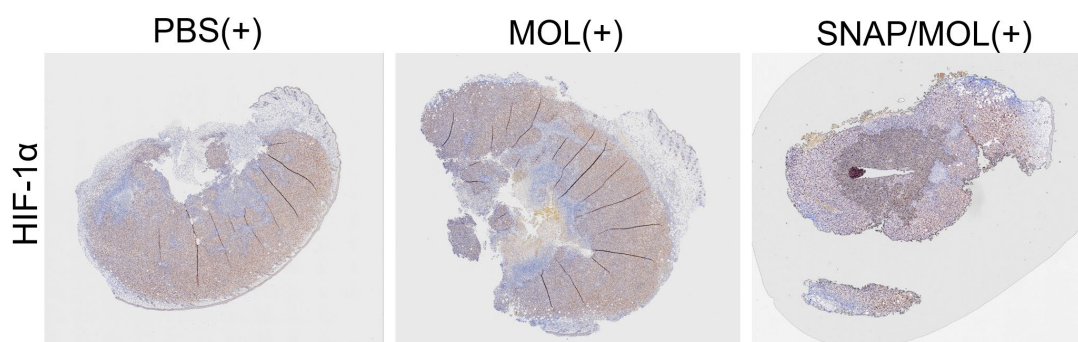


**Figure S40.** Immunohistochemistry analysis of HIF-1 $\alpha$  staining in whole tumors.